Bulletin of the Seismological Society of America, Vol. 97, No. 1A, pp. S232–S248, January 2007, doi: 10.1785/0120050607

High-Frequency Tsunami Signals of the Great Indonesian Earthquakes of 26 December 2004 and 28 March 2005

by Jeffrey A. Hanson, Colin L. Reasoner, and J. Roger Bowman

Abstract Tsunamis generated by the great Indonesian earthquakes of 26 December 2004 (M_w 9.3) and 28 March 2005 (M_w 8.6) produced high-frequency (>5 mHz) dispersed signals recorded by hydrophone stations offshore from Diego Garcia and Cape Leeuwin, Australia, and by many seismic stations in the Indian Ocean and on the coast of Antarctica. For the first and greater earthquake, the dispersed energy is commonly observed to 30 mHz and, in one case, to 60 mHz. The high-frequency signals are consistent with being generated at pointlike sources. The earliest arriving tsunami signals originate from a point near 4.3° N, 93.8° E, determined using event-to-station distances estimated by matching predicted dispersion to observations. The location is further constrained with azimuth estimates from an array of hydrophones. Fine structure in the tsunami signal indicates a second high-frequency source just south of Great Nicobar Island near 6.5° N, 93.6° E. The point sources are located close to the maximum slip area determined in several other seismic and tsunami studies. The dispersion of much later-arriving energy is consistent with travel over longer paths, and matches predictions for reflections of the tsunami from bathymetric features in the Indian Ocean basin. For the 28 March 2005 tsunami, the high-frequency dispersion is observed at the Diego Garcia hydrophone station and the AIS seismic station, and tsunami signals without apparent dispersion are seen at four other seismic stations. Phase velocities estimated at hydroacoustic stations agree with linear dispersion theory at frequencies above 12 mHz.

Introduction

The great Sumatra Earthquake of 26 December 2004 (M_w 9.1 to 9.3) was followed by an M_w 8.6 earthquake that ruptured an adjacent fault segment on 28 March 2005 (Lay *et al.*, 2005). The first earthquake ruptured a 1200- to 1300-km-long segment of a subduction plate boundary with fault displacements up to at least 20 m in some areas. The earthquake and subsequent tsunami were responsible for more than 200,000 deaths in at least 13 countries. The second event ruptured 300 km of the plate boundary to the southeast of the first earthquake's rupture zone. These represent the two largest earthquakes in the past 40 years, and their signals were recorded with unprecedented fidelity by global seismic, hydroacoustic, and infrasonic networks. Both earthquakes generated tsunamis that affected the entire Indian Ocean basin, and the December tsunami was recorded worldwide (Merrifield *et al.*, 2005; Titov *et al.*, 2005).

Signals of every kind from the great earthquakes and resultant tsunamis were recorded around the Indian Ocean basin on a wide variety of instruments. Seismic body waves and surface waves were measured on seismometers, hydrophones (deGroot-Hedlin, 2005), and microbarometers of infrasound stations (Garcés *et al.*, 2005). Acoustic *T* phases of the mainshocks and aftershocks were observed on hydrophones (deGroot-Hedlin, 2005; Tolstoy and Bohnenstiehl, 2005) and infrasound stations (Garcés *et al.*, 2005). The tsunami itself was directly measured using tide gauges (Fine *et al.*, 2005; Merrifield *et al.*, 2005), satellite altimetry (Fine *et al.*, 2005; Gower, 2005; Kulikov, 2005), seismic data (Hanson and Bowman, 2005; Yuan *et al.*, 2005), and hydroacoustic data (Graeber *et al.*, 2005; Hanson and Bowman, 2005).

This article concentrates on measurements of relatively high-frequency tsunami signals using data from hydroacoustic and seismic stations in and around the Indian Ocean basin (Figs. 1 and 2). It extends the results of Hanson and Bowman (2005) with a more detailed and quantified analysis of the dispersed tsunami signals, data from additional seismic stations, and data from the 28 March 2005 event. Three types of signals from the tsunami are observed that are consistent with predictions of models for ocean gravity waves. The first signal type is the strongest and represents the direct arrival of the tsunami from the area of greatest fault slip. The second type is weaker and follows shortly after the first signal, and may be the direct arrival of tsunami energy from a secondary area of large fault slip or from near-source reflections. The

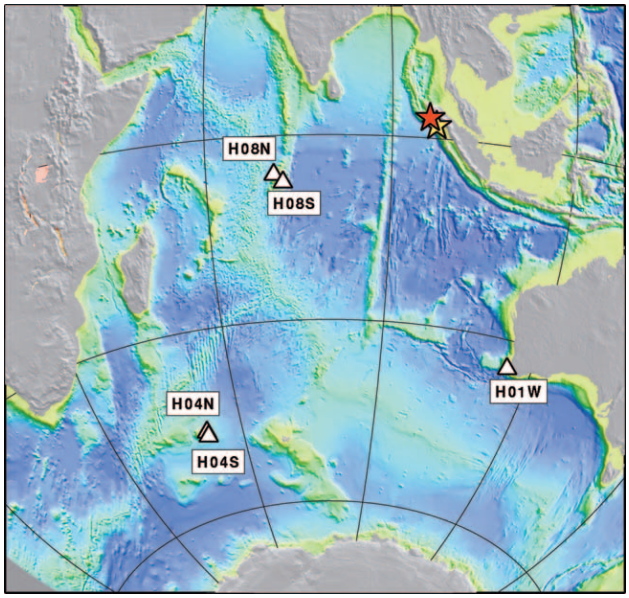

Figure 1. IMS hydroacoustic stations in the Indian Ocean. White triangles are hydroacoustic triads (H01W, H04N, H04S, H08N, and H08S). The epicenters are shown for the 26 December 2004 earthquake (red star) and the 28 March 2005 earthquake (yellow star).

third signal type arrives considerably after the first two and exhibits much greater dispersion. These signals are interpreted to be tsunami waves reflected from ocean bathymetry, whose dispersion is greater because of the longer travel paths.

Tsunamis are ocean gravity waves with very long wavelengths, in general. In deep water, they have a small vertical displacement, which allows for a linear solution of the wave equation (e.g., Lamb, 1932). This leads to the well-known dispersion relation for gravity ocean surface waves:

$$\omega^2 = g \cdot k \tanh(k \cdot d),$$

where, ω is angular frequency, k is wave number, d is water depth, and g is the acceleration of gravity. Phase and group velocities can be defined as:

$$c_p = \frac{\omega}{k} = \sqrt{\frac{g}{k}\tanh(kd)}$$
$$c_g = \frac{\partial\omega}{\partial k} = \frac{\omega}{2k}\left(1 + \frac{2kd}{\sinh(2kd)}\right). \quad (1)$$

Tsunamis are often treated using the shallow water (nondispersive) approximation, that is, $\tanh(kd) \rightarrow kd$ for $kd \ll 1$, and wind-driven ocean waves are treated using the deep-water approximation, that is $\tanh(kd) \rightarrow 1$ for $kd \gg 1$. However, the observations presented here span both of these regimes. Figure 3 shows phase and group velocities from (1) as a function of frequency calculated at a series of different water depths. The shallow- and deep-water approximations for 4000 m depth are shown for comparison. Because the signals examined range from 1 to 60 mHz, equation (1) is used to predict phase and group velocities. Most of the waves that are examined here have traveled almost exclusively in water depths of 3000 m or more, and so the dispersion is almost entirely controlled by the distance traveled.

The typical tsunami frequency band ranges from about 0.14 to 8 mHz. The frequency of the earthquake-induced tsunami is controlled by the earthquake rupture, the earthquake depth, and the depth of water above the seafloor displacement. Surface waves with wavelengths that are short compared with the water depth cannot be excited by a seafloor disturbance. In this way, the water layer acts as a low-pass filter of the seafloor disturbance. The attenuation is proportional to $1/\cosh(kd)$ (e.g., Webb *et al.*, 1991). This leads to a rule of thumb from Ward (2001) that "only wavelengths of the uplift source that exceed three times the ocean depth contribute much to tsunamis." This rule cannot be taken too literally because the attenuation function is continuous and depends on the amplitude and frequency content of the source function of the event.

The hydrophones used in this study are located 1000 to 1300 m below the ocean surface. Because of this, the pressure signal from surface-gravity waves are attenuated at higher frequencies, similar to the source attenuation due to water depth. This limits the hydrophones' observations of surface-gravity waves to frequencies less than approximately 30 mHz. For example, a surface-gravity wave recorded on a hydrophone 1300 m below the sea surface in 1700-m-deep water will have attenuated 95% at approximately 27 mHz. The seismic stations record ground motion induced by the tsunami. The response of the ground to the tsunami is likely a complex function of the local bathymetry and the distance and elevation to the seismic station. This limits the ability to meaningfully compare amplitudes at one seismic station with another, but separate signals from similar directions at a single seismic station can be directly compared.

Data

Hydrophone and seismic data from stations in and around the Indian Ocean are analyzed to observe the 26 December 2004 and 28 March 2005 tsunamis. The hydrophone stations used are part of the International Monitoring System's (IMS) hydroacoustic network. Each hydrophone station consists of one or two "triads" of instruments, and each triad consists of three hydrophones arranged in roughly equilateral triangles with 2-km sides (Fig. 4a). In general, the hydrophones are positioned 50 to 200 km from shore. They are attached to anchors on the seafloor and are floated to the sound channel axis by buoys. This places the Diego Garcia and Cape Leeuwin hydrophones approximately 1300 m below the ocean surface. Cape Leeuwin has a single triad

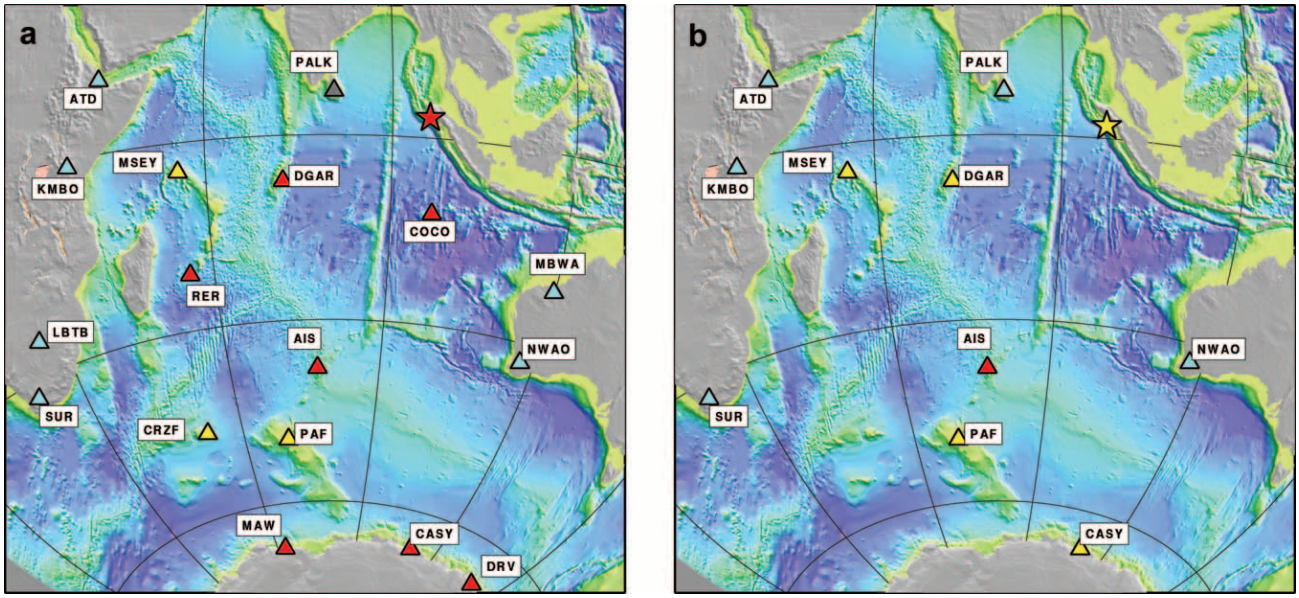

Figure 2. Seismic-recording stations around the Indian Ocean used in this study. (a) 26 December 2004 event. (b) 28 March 2005 event. Triangles are seismic stations, color coded to indicate no observed tsunami signal (cyan), a nondispersive tsunami signal, that is, $\ll$5 mHz (yellow), or both nondispersive and dispersive tsunami signals, that is, >5 mHz (red). For the December tsunami, the seismic signal at PALK obscures observations of a possible tsunami signal. Many of the island stations that do not observe the higher-frequency dispersed signal, do observe the large low-frequency tsunami. The stars indicate the earthquake epicenters.

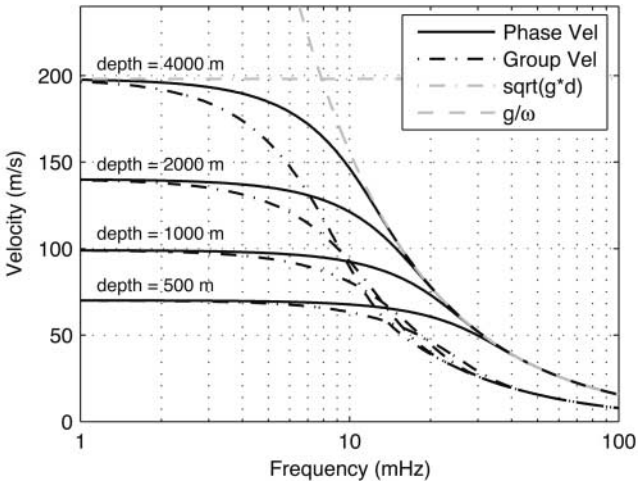

Figure 3. Theoretical dispersion curves for ocean-gravity waves. Phase velocity and group velocity for a variety of ocean depths are shown. Also included is a comparison of phase velocity with the shallow- and deep-water approximations. In the case of 4000-m-deep water, the deep-water approximation closely matches the dispersion above 15 mHz.

(H01W) located southwest of Australia. The Diego Garcia station has two triads positioned northwest (H08N) and southeast (H08S) of the island. The Crozet Island station also has two triads, north (H04N) and south (H04S) of the island, but only two hydrophones of each triad were operational. A fourth station at Juan Fernandez, Chile, in the Pacific Ocean is not shown. It had one operational triad north (H03N) of the island and a nonoperational triad south (H03S). The triads of all stations have a much larger interelement spacing (~2 km) than typical hydrophone arrays. This large spacing can cause coherence or spatial aliasing problems for array processing of typical hydroacoustic signals (Hanson *et al.*, 2002; Hanson and Bowman, 2006). However, this extended baseline is a fortuitous design for analyzing the long-wavelength tsunami signals.

Data from the Global Seismic Network of seismic stations surrounding the Indian Ocean (Fig. 2) are also analyzed. Several of these seismic stations, for example, DGAR on Diego Garcia and COCO on the Cocos (Keeling) Islands, are essentially at sea level. Seismometers that are part of the Global Seismic Network typically have flat-frequency response in velocity from 10 to 30 mHz up to 5 to 10 Hz. The stations can record ground motion to extremely long periods including earth tides (e.g., Lay and Wallace, 1995). Data from the long-period or very-long-period channels (LH or VH) are used, sampled at 1-sec and 10-sec intervals, respectively.

The IMS hydrophone stations were designed to record signals from 1 to 100 Hz, making them less than ideal for recording tsunami signals. Four of the six hydrophone triads (H01W, H03N, H08N, H08S) have the identical sensor design, whereas the Crozet Island sensors (H04N and H04S) have a different design and hence a different frequency re-

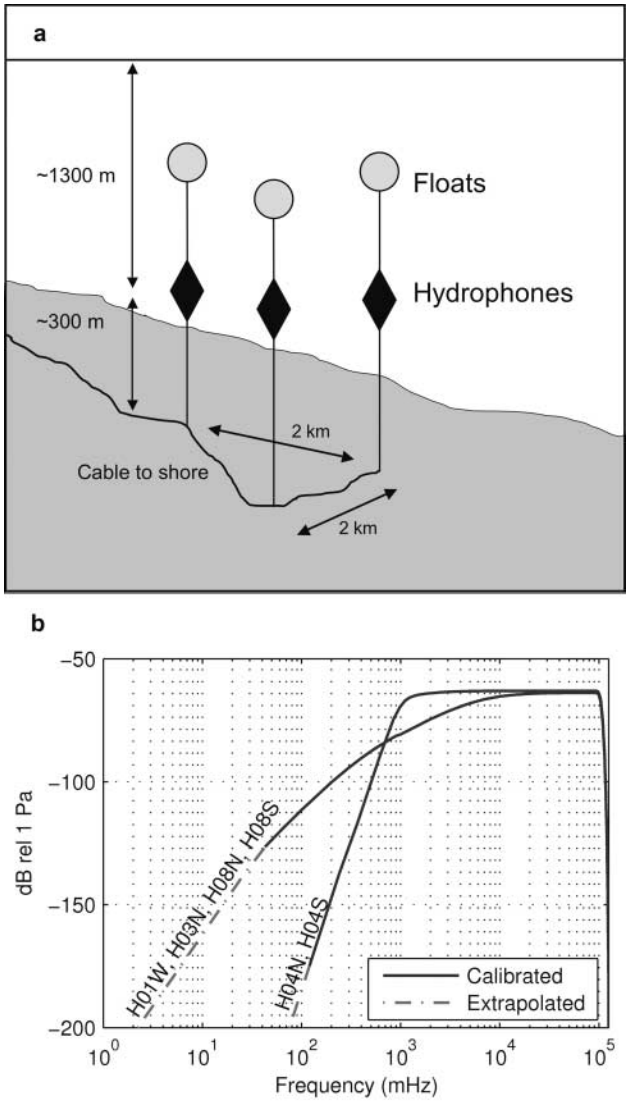

Figure 4. Characteristics of hydrophone triads. (a) Cartoon of hydrophone deployment at H08S. Three hydrophones, tethered to the seafloor, are floated into the sound channel axis. A fiber optic cable returns the data to shore. The hydrophones in this case are at approximately 1300 m below the sea surface and 300 m above the seafloor and separated by approximately 2 km. (b) Frequency response of the hydrophone triads to pressure. The responses have been extrapolated to low frequencies based on the theoretical response of the mechanical and electrical systems. The response at Diego Garcia (H08N/S) and Cape Leeuwin (H01W) falls off more gradually below 1 Hz than the response at Crozet (H04N/S).

sponse. Figure 4b shows the hydrophone frequency responses, provided by the International Data Centre (IDC) down to 100 mHz. We obtained calibration information down to 40 mHz for the instruments at H01W, H03N, H08N, and H08S and extrapolated the response to 1 mHz based on the instrument characteristics (N. Gholson, personal comm., 2006). The response below 100 mHz at H04N and H04S is extrapolated from higher frequencies. They have responses that are almost flat between 1 and 100 Hz, but fall off sharply below 1 Hz. In contrast, the response of the other hydrophone stations rolls off below 10 Hz, but declines more gradually at lower frequencies than for the Crozet stations. The frequency responses suggest that all the hydrophone stations would have comparable sensitivity in the passband relevant for recording in-water explosions and submarine earthquakes, but that Cape Leeuwin (H01W), Diego Garcia (H08N, H08S), and Juan Fernandez (H03N) would have substantially greater sensitivity for recording lower-frequency signals, such as tsunamis, than the sensors at H04N and H04S. However, the sensitivity for all the hydrophones is greatly diminished at long periods compared with their intended passband. There is indication that the instrument response is correct to better than an order of magnitude at about 10 mHz. Okal, *et al.* (2006) compared the spectral amplitude of the vertical displacement of Rayleigh wavetrains recorded at H08S1 and DGAR, which are separated by 25 km. After deconvolution of the instrument response, the two spectra agreed to within 10% down to 15 mHz and 20% down to 10 mHz.

Observations

Our observations are largely based on spectrograms estimated from the hydrophone or seismometer time series. The hydrophone time series are decimated from a 250-Hz sampling rate to 1 Hz. The seismic time series are either sampled at 0.1 Hz (VH channels) or 1 Hz (LH channels). The spectrograms are computed using a sliding time window with three-quarters overlap. The time window is chosen so that the dispersion of a shallow-water wave will be equal to one discreet frequency step for each timestep. This leads to a time window equal to $\sqrt{4\pi\Delta/g}$, where Δ is the approximate distance between source and receiver. For the hydroacoustic data, the spectrograms of each individual hydrophone in a triad are averaged. The spectrograms for the seismic data are computed using the two horizontal components. The horizontal components displayed significantly higher-amplitude tsunami signals than the vertical components. This is likely due to the tsunamis' largely horizontal particle displacement, which at low frequencies can be an order of magnitude larger than the vertical motion (Ward, 2001). No significant difference is found between averaging the individual spectrograms of the two horizontal components and computing the spectrogram from a single horizontal component rotated to maximize amplitude of the low-frequency arrival. A time-frequency filter is applied to all spectrograms to reduce the variance of the spectra. To enhance the tsunami signal, an ambient-noise spectrum is estimated from the time series, which is then removed from each time window of the spectrogram.

Many seismic stations display clear dispersed signals in the spectrograms. In contrast, some seismic stations do not exhibit a dispersed signal, but do record the low-frequency

portion of the tsunami. This portion of the signal is most easily observed using bandpass filters of the time series data. A series of filters are applied to examine all seismic data for evidence of a signal consistent with the tsunami whether or not a dispersed signal is visible in the spectrograms.

26 December 2004 Earthquake

Figure 5 shows spectrograms for 48 hr for the three hydrophone triads that recorded the tsunami: H01W, H08N, and H08S. The left-hand panels show the spectrogram without interpretation. High amplitudes shown in red at the left margin of the Diego Garcia spectrograms and at the right edge of the H01W spectrograms are seismic phases from aftershocks. Each spectrogram is characterized by a dominant signal slashing diagonally up from below 5 mHz to above 20 mHz over a period of 24 to 36 hr. We refer to this dispersive signal as a "chirp." On the right-hand panels, the expected dispersion curves for a source at 4.3° S, 93.8° E are superimposed onto the spectrograms. In addition, a few curves representing prominent reflectors in the Indian Ocean are included on some panels.

The onset of the tsunami chirp at H08S corresponds with the onset of the tsunami recorded on the Diego Garcia-D tide gauge (Hanson and Bowman, 2005), which is part of the Global Sea Level Observing System (GLOSS No. 026). The slope of the dominant chirp is steeper for H08N and H08S than for H01W because the source–receiver path is longer to Cape Leeuwin (~4800 km compared with ~2800 km to Diego Garcia), and therefore the signal has had more opportunity to disperse. The dispersion curves are computed using the average ocean depth along the source–receiver path. This is a good approximation for H08S and H08N, but it begins to fail for H01W at low frequencies because the path crosses shallower bathymetry that refracts the low-frequency energy. Adjusting the ocean depth used in the dispersion calculation can improve the fit at lower frequencies, but it still does not account for refraction effects and thus will not match the data perfectly. Note that waves that meet the deep-water approximation along essentially the entire path are not sensitive to the water depth. In this case, distance traveled is the only free parameter to adjust.

Energy is seen arriving at each triad in the Figure 5 spectrograms after the dominant signals. We interpret these lower-amplitude chirps as reflected tsunami signals. They have a shallower slope and later arrival time because the reflected signal paths are longer than the direct paths. Multiple branches are the result of multiple reflection points.

No tsunami signals are observed at either of the Crozet triads, H04N and H04S. This is likely to be a consequence of the frequency response of their sensors, which are much less sensitive at extremely low frequencies (Fig. 4b). No

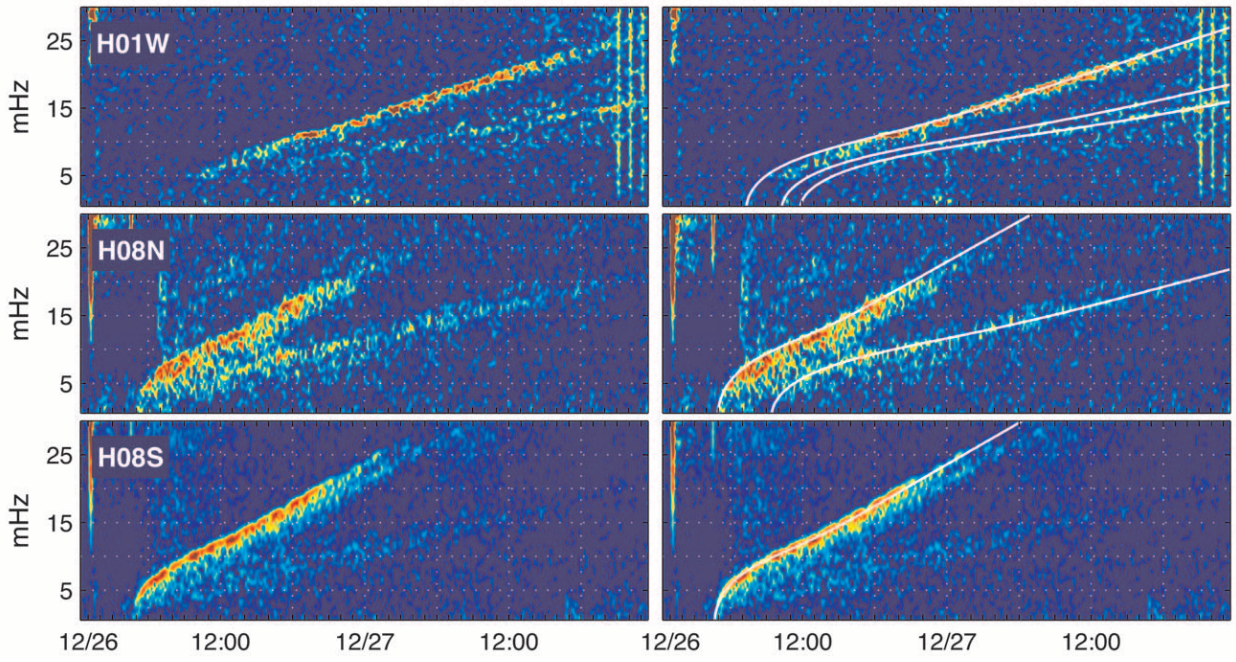

Figure 5. Spectrograms for 48 hr showing the observed and theoretical dispersion at hydrophones in the Indian Ocean for the 26 December 2004 earthquake. The left-hand column shows observed spectrograms for three hydroacoustic stations. The right-hand column contains the same spectrograms overlaid with theoretical dispersion curves for some direct and reflected tsunami arrivals assuming an average ocean depth of 4500 m. The color scale is adjusted to emphasize the tsunami signals such that the seismic arrivals are saturated red. Data gaps and quality problems cause the vertical strips.

tsunami signals are observed at hydrophone station H03S in Chile, presumably because of the long range and lack of direct path from the source.

Spectrograms and theoretical dispersion curves are displayed in Figure 6 for seismic stations on islands or near the coast in the Indian Ocean basin. Some stations show clear chirps from the direct tsunami and others do not, as summarized in Table 1. Those having clear tsunami signals are AIS, CASY, COCO, DGAR, MAW, RER. CRZF and DRV have weak chirps. Other seismic stations (not shown) exhibited very weak or no chirps. MSEY and PAF do not exhibit chirps, but low-pass filtering of the data shows that they do record the main tsunami signal. The other stations from Figure 2 (ATD, KMBO, LBTB, MBWA, NWAO, and SUR) do not show evidence of tsunami signals. The signal at DGAR on Diego Garcia exhibits the same dispersion of direct and reflected phases as the hydrophone stations H08S and H08N. It appears that whether a tsunami signal is observed at a seismic station is directly related to the station's elevation and its proximity to shore. Lower-elevation stations, which are generally closer to shore, have an increased probability of observing the tsunami.

Several seismic stations show evidence of reflected tsunami signals in addition to the direct arrivals. At Cocos (Keeling) Islands, the reflections at station COCO are more evident than the direct tsunami wave. Stations AIS and CASY record signals that arrive later than the direct signal. Several stations, such as AIS, DRV, and MAW exhibit higher energy in a broad zone to the right of the first-arriving tsunami. Some of the energy in the spectrograms resembles that of a composite of discrete dispersion curves. The station furthest from the earthquake epicenter at which a chirp signal has been observed is station HOPE on South Georgia Island in the southern Atlantic Ocean, approximately 12,900 km from the source. The chirp is clearly visible up to 15 mHz. The entire dispersed chirp arrives late compared with the theoretical dispersion, which is likely due to the wave crossing shallow-water areas between South Africa and Antarctica, such as the Crozet Islands and associated seamounts.

The previous spectrograms have had the background noise removed to better observe the dispersed signal. To place the signal in terms of physical units, computed spectra of the ambient noise and dispersed tsunami signal at H08S, H01W, and AIS are shown in Figure 7. The spectra are corrected for instrument response. The hydrophone response has a high uncertainty because the instruments were not designed or calibrated for these frequencies (N. Gholson, personal comm., 2006). The spectral shape and amplitude at the hydrophones above 100 mHz are characteristic of bottom pressure measurements at other deep-water sites (e.g., Webb *et al.*, 1991). The lack of structure in the spectra at lower frequencies probably indicates that instrument noise dominates the ambient-noise level. However, a slight hump in the H08S spectra at about 10 mHz may be due to infragravity waves. The signal at both hydrophone stations disappears into the noise at 30 mHz, which is consistent with the expected surface-wave attenuation with depth. The signal at AIS disappears at ~60 mHz as the noise increases toward the microseism band.

28 March 2005 Earthquake

The 28 March 2005 earthquake (M_w 8.6) was smaller than the 26 December 2004 event (M_w 9.3) and generated a significantly smaller tsunami. H08S is the only hydroacoustic station that observes a dispersed tsunami signal (Fig. 8). Regular energy bursts of unknown origin at H01W obscure any tsunami signal that may have been present. Seismic stations are also examined for tsunami signals. Station AIS on Amsterdam Island is the only seismic station found with a dispersive tsunami signal in its spectrogram for the 28 March 2005 earthquake (Fig. 8). There is a signal that might be a reflected phase following the direct arrival, but it is too weak to assert with confidence.

Observation of dispersive tsunami signals in spectrograms requires that the tsunami signal have a high signal-to-noise ratio (SNR) over a range of frequencies. Yuan *et al.* (2005) filtered horizontal-component seismograms in low-frequency bands for the 26 December 2004 tsunami. This approach accommodated lower SNR and allowed them to identify tsunami signals at seven seismic stations. This approach is applied to the 28 March 2005 event as illustrated in Figure 9 and summarized in Table 2. The lowest-frequency bands, 0.2 to 0.7 mHz and 0.5 to 1.0 mHz, revealed the tsunami signals at AIS, CASY, DGAR, MSEY, and PAF.

Array Processing

The hydrophone triads allow for coherent array processing of the incident tsunami wave field to determine arrival azimuths and phase velocities. FK spectra are computed for the time series from the H08S triad using a series of overlapping time windows (Fig. 10). The time windows were 1.5 hr long. The FK spectra are computed with a 10-mHz bandwidth centered at a frequency estimated from the theoretical group velocity dispersion for the direct arrival. The FK spectrum is computed for each window, and the maximum peak is used to compute the arrival azimuth and phase velocity that are plotted in Figure 10 versus the center frequency. The azimuth varies from 105° below 4 mHz (corresponding to the onset of the tsunami) to ~60° above 17 mHz. The phase velocity is approximately constant at 100 m/sec between 5 and 12 mHz, and it decreases smoothly above 12 mHz. These observations, are in general, consistent with the earthquake location and near-receiver refraction effects. Figure 11 shows the location of the H08S triad with the surrounding bathymetry. The water depth at the sensors is approximately 1600 m. The observed dispersion is consistent with a wave that has traveled 2700 km through 4000+ m water, but the FK measures the local-phase velocity, and not the average-phase velocity of the source–

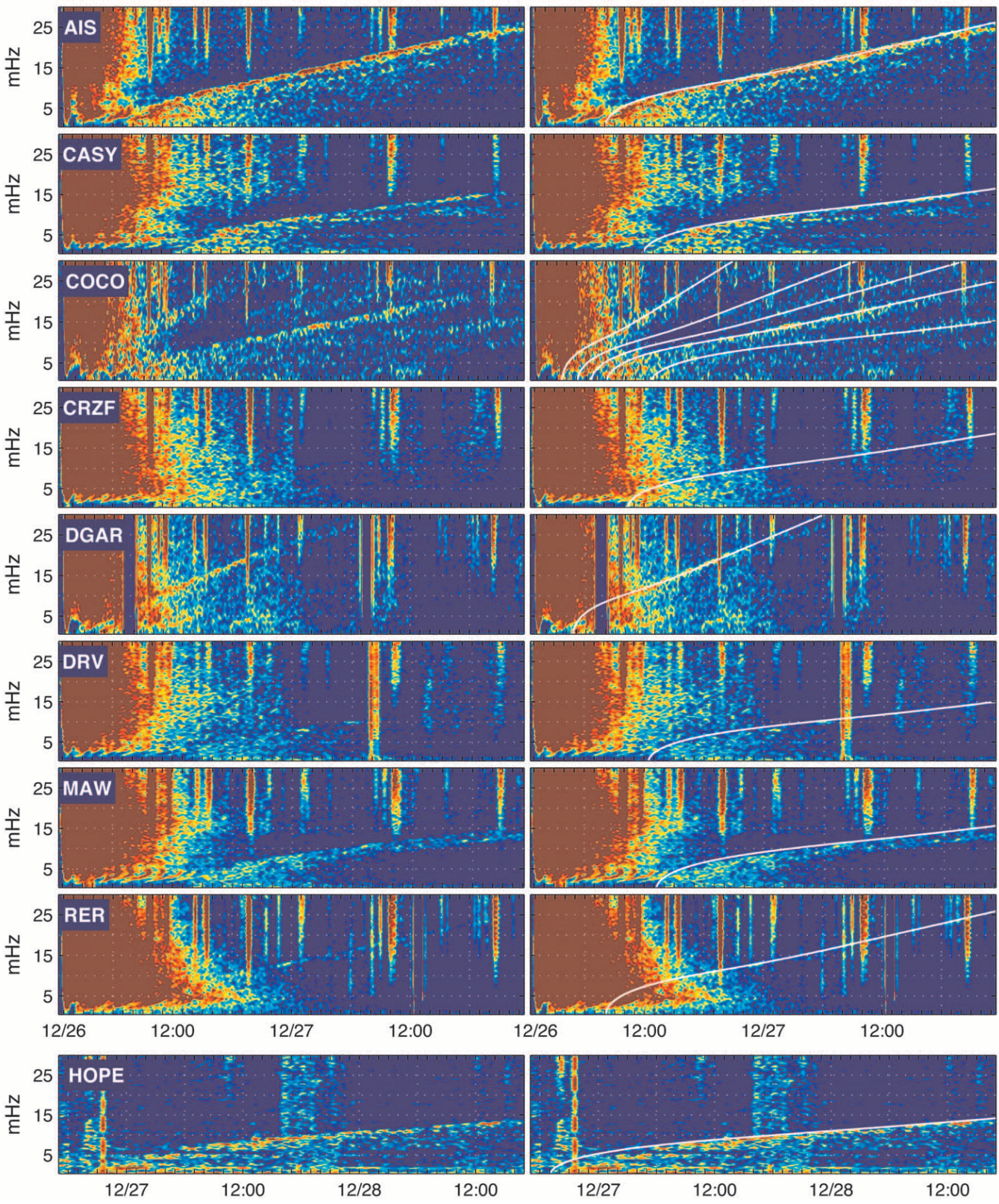

Figure 6. Spectrograms for seismic stations in and near the Indian Ocean basin for the 26 December 2004 earthquake. The ambient-noise spectrum has been removed from the spectrograms to enhance the dispersed signal. The left-hand column shows the spectrograms only, and the right-hand column adds the theoretical dispersion curve. Red tones in the first 10 to 12 hr and vertical red strips are seismic phases from the mainshock and aftershocks. Direct tsunami signals are identified at all stations shown. Distinct reflected tsunami signals are clearly observed at COCO. Less distinct reflections are seen at AIS and DGAR.

Table 1
Summary of Seismic Spectrogram Observations for the 26 December 2004 Tsunami

Code	Name	Elevation (m)	Distance to Coast (km)	Observations of Tsunami
AIS	Amsterdam Island	36	<10	Clear dispersed signal, reflections
ATD	Arta Tunnel	610	900	No signal
CASY	Casey, Antarctica	154	20	Clear dispersed signal
COCO	Cocos (Keeling) Islands	1	<10	Weak dispersed direct signal, clear reflections
CRZF	Port Alfred, Crozet Islands	140	<10	Clear nondispersed signal
DGAR	Diego Garcia	1	<10	Clear dispersed signal
DRV	Dumont d'Urville (Pointe Geologie, Adelie)	40	60	Very weak dispersed signal
HOPE	Hope Point, South Georgia, Island	20	<10	Clear dispersed signal
KMBO	Kilima Mbogo, Kenya	1940	400	No signal
LBTB	Lobatse, Botswana	1028	700	No signal
MAW	Mawson, Antarctica	12	40	Clear dispersed signal
MBWA	Marble Bar, Western Australia	185	160	No signal
MSEY	Mahe Island, Seychelles	475	<10	Clear nondispersed signal
NWAO	Narrogin, Western Australia	265	150	No signal
PAF	Port'aux Francais, Kerguelen	17	<10	Clear nondispersed signal
PALK	Pallekele, Sri Lanka	460	140	Indeterminate
RER	Riviere de L'Est, La Reunion	834	<10	Clear dispersed signal
SUR	Sutherland, Republic of South Africa	1760	220	No signal

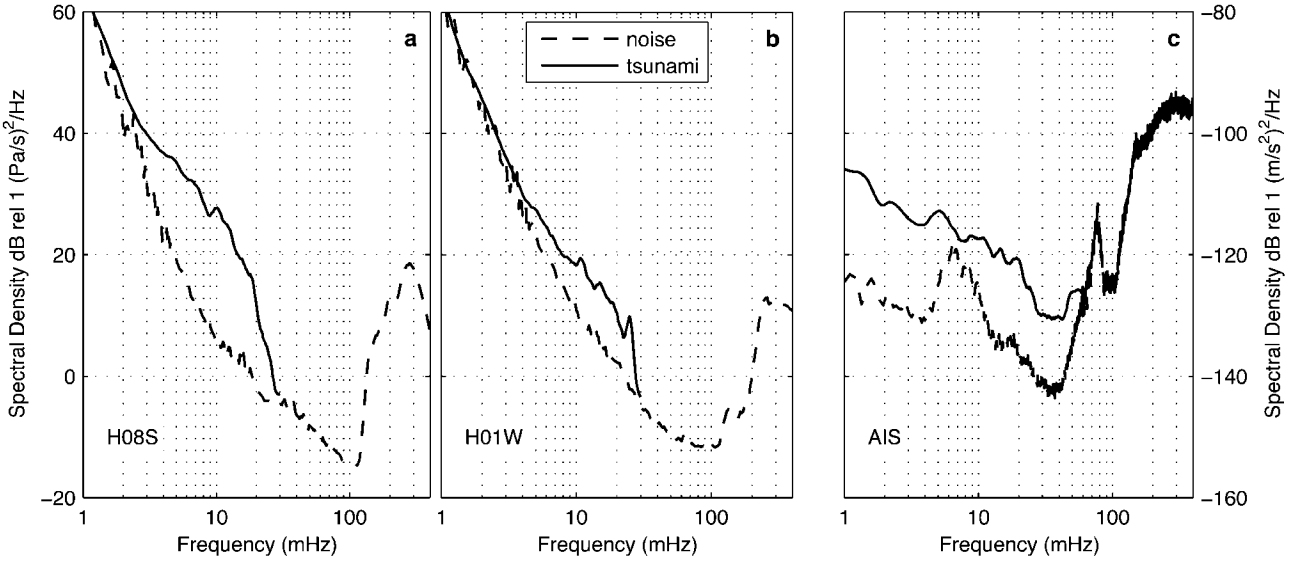

Figure 7. Power spectral density estimates of the noise and tsunami signal at H08S, H01W, and AIS corrected for instrument response. The instrument response for the hydrophones below 40 mHz is uncertain because no calibration tests have been conducted at such low frequencies. The spectral shape and amplitude of the hydrophone signals above 100 mHz is physically reasonable and likely is representative of ambient ocean noise. Below 100 mHz instrument noise probably dominates the noise spectrum. The tsunami spectra are estimated along the expected signal dispersion.

receiver path. The theoretical curve in Figure 10 is the phase velocity predicted for 1600-m-deep water using equation (1). The phase velocities estimated above 12 mHz agree with theory. At frequencies less than 12 mHz, the estimates deviate from theory. The reason for this is not clear. It may be that the SNR has become too small or that the time or frequency windows used are not optimal at these frequencies. It is also possible that multipathing is affecting the results. In addition, it is possible that infragravity waves leaking from trapped waves along coasts are creating an interfering source (e.g., Oltman-Shay and Guza, 1987). The azimuth variations are understandable because the tsunami is expected to refract to the west as it reaches the Chagos Archipelago. This will affect lower frequencies more and higher frequencies less until the wavelengths are short enough that they do not feel the moderately deep bathymetry.

Secondary signals are observed on H08S with azimuths around 240° that are interpreted to be reflections from the

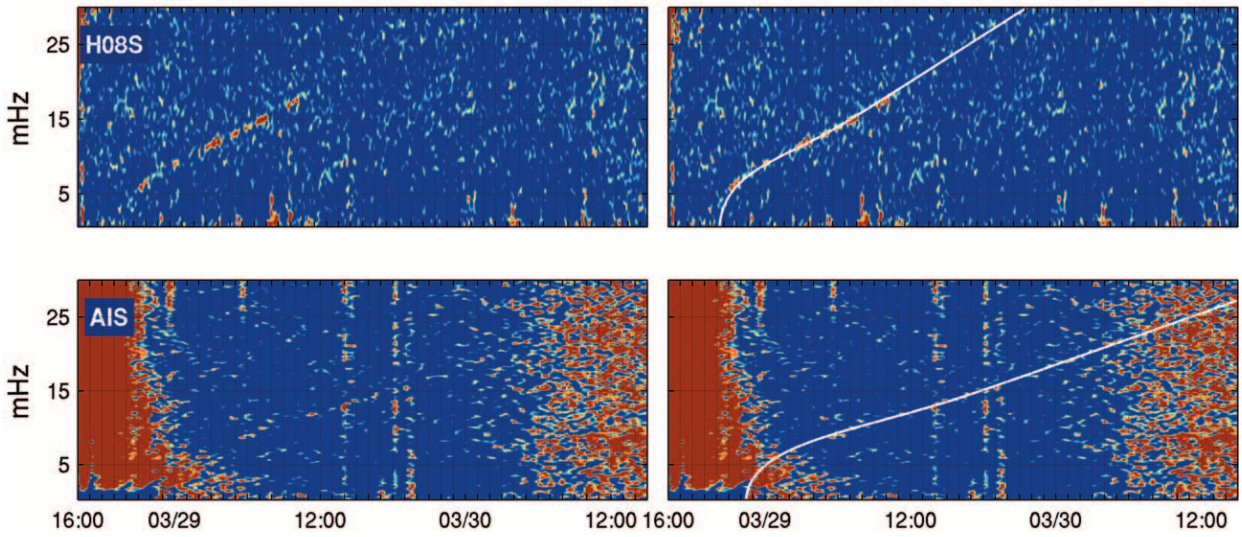

Figure 8. Spectrograms from the Indian Ocean for the 28 March 2005 event. The left-hand column shows the spectrograms only. In the right-hand column the theoretical dispersion curve is overlaid on top. H08S was the only hydrophone to have a convincing tsunami signal. The chirp signal at the seismic station AIS is weak, but visible between 8 and 15 mHz.

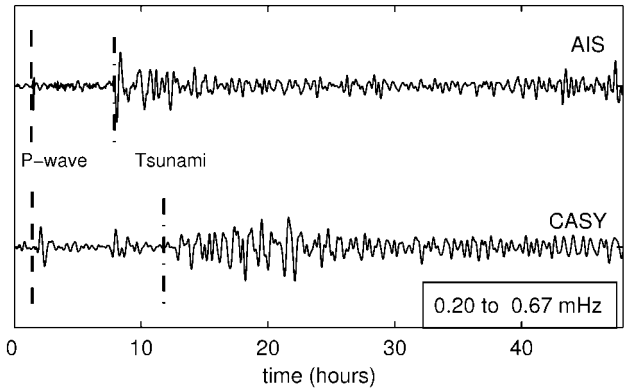

Figure 9. Filtered horizontal-component seismograms for AIS and CASY. The waveforms are filtered between 0.20 and 0.67 mHz. The predicted *P* wave and tsunami arrival times are indicated with vertical lines. A clear tsunami signal is observed at both stations.

Table 2
Summary of Observations from Filtered Seismograms for the 28 March 2005 Tsunami

Code	Observations of Tsunami
AIS	Clear dispersed signal
ATD	No signal
CASY	Clear nondispersed signal
DGAR	Clear nondispersed signal
KMBO	No signal
MSEY	Clear nondispersed signal
NWAO	No signal
PAF	Clear nondispersed signal
PALK	No signal
SUR	No signal

Mascarene Plateau. The direct arrival at H08N is not coherent because the Chagos Archipelago causes severe multipathing, but a reflected arrival from the Mascarene Plateau is observed at an azimuth of approximately 270°.

Spectrogram Fine Structure

The spectrograms from the hydrophone stations and several seismic stations contain more detailed structure than apparent upon initial examination. Above 10 mHz, distinct bands that appear to be separate chirp signals can be discerned. To better observe this fine structure, the spectrograms are transformed by using a "reduction frequency," which is similar to a reduction velocity of a record section plot used in seismic surveying. The reduction is achieved by shifting each column of the spectrogram by $T \cdot g/4\pi\Delta$, where T is time relative to the earthquake origin time, and Δ is the source–receiver distance. This shift corresponds to the expected arrival time of a deep-ocean wave having propagated a distance Δ. Figure 12 displays the results for stations H08S and AIS. Theoretical dispersion curves that match two of the more prominent bands are overlaid on the spectrograms. We interpret the individual bands to represent distinct high-frequency tsunamis that either originate in different locations or travel a different path via reflection. Distinct high-frequency sources could arise from variations in the bathymetry or variations in the slip along the fault.

Precise measurements of the fine structure are obtained by summing power along theoretical dispersion curves. Higher frequencies are weighted more because the one-dimensional calculation is more accurate at high frequencies. Frequencies below 8 mHz are not included because these are

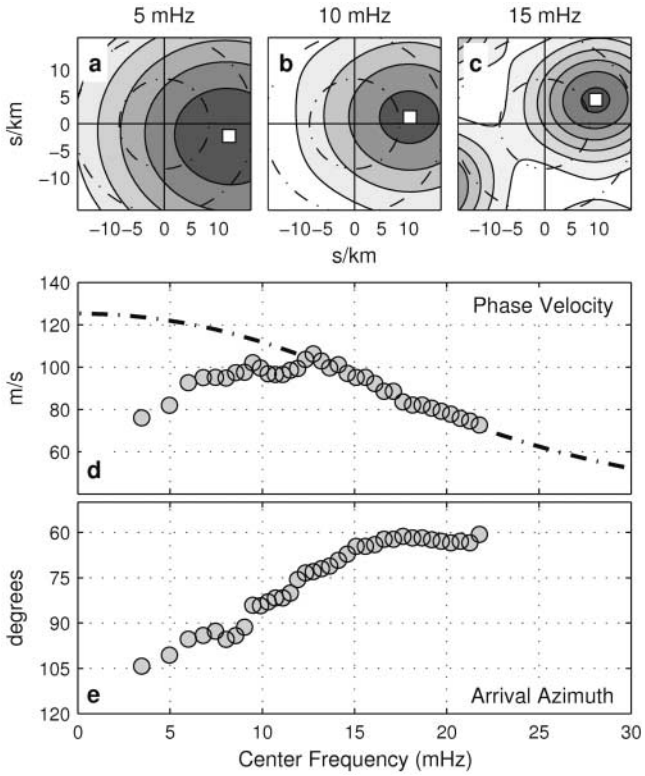

Figure 10. FK analysis of H08S observations for the December tsunami. (a–c) FK spectrum in slowness space. The white square indicates the maximum peak in the spectrum. The FK was computed using a 1.5-hr time window and a 10-mHz frequency band centered at the frequency determined from the theoretical group velocity-dispersion curves. (d) Phase velocity determined from the peak in the FK spectrum plotted as a function of center frequency. The dashed curve is the theoretical phase velocity for 1600-m-deep water (the approximate water depth at H08S). (e) Azimuth determined from the peak in the FK spectrum. The arrival azimuth begins near due east, but swings to approximately 60° (the expected azimuth) at higher frequencies. The azimuth variation is likely due to refraction from the shoaling bathymetry (see Fig. 11), but does not explain the phase velocity deviations at low frequencies.

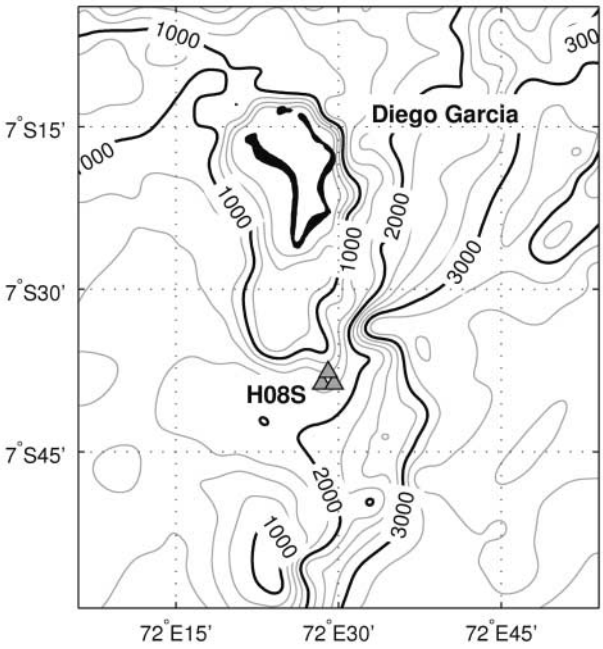

Figure 11. Bathymetry surrounding H08S triad with contours in meters. The tightly clustered triangles southeast of Diego Garcia represent the individual triad elements. The shoaling bathymetry will cause the tsunami wave to refract clockwise from the deep-water propagation direction (northeast to southwest). The higher-frequency waves do not "feel" the bathymetry as much and thus are less refracted.

more affected by bathymetry, and, in any case, closely spaced sources would not separate well at these frequencies. Figure 13 shows the normalized power summations as a function of dispersion distance for three stations. The plots show the fine structure of the initial arrival at H08S and AIS. Summation results from a later-arriving signal (reflection) have been included for station H01W. Table 3 presents the results including error estimates.

Source and Reflector Location Estimates

The distance estimates determined previously at different stations can be used together to estimate source locations. Assuming there is no blockage between the tsunami source and the stations, the first arrival must be from a tsunami source as opposed to a reflection. However, secondary arrivals could be from either a displacement source or a reflection of the first source. We have chosen to use the first arrivals at H08S, AIS, and H01W to constrain the source location of the first arrival. These three stations have high-quality data measurements and are relatively free of bathymetric complications between the source and receiver. Distances and errors estimated from the high-frequency tsunami signal can be directly translated to annuli that surround the station. Figure 14 shows the annuli for the three stations in the region of the fault rupture. Azimuthal constraints estimated for H08S are included. The distances to the annuli are computed using the WGS-94 ellipsoidal earth model.

The destructive December 2004 tsunami has a distributed source that has been modeled using data from tide gauges and satellite measurements (e.g., Tanioka *et al.*, 2006; Fujii and Satake 2007; Piatanesi and Lorito, 2007). At the frequencies used in these studies, the source must be considered as distributed across long distances. The high-frequency tsunami data presented here suggest the origin of these signals is more pointlike in nature. First, the limited width of the dispersed signals indicates a narrow source. Second, the first arrivals at stations H01W, AIS, and H08S constrain the source toward the southeast, southwest, and west, respectively. In addition, a strong reflection appears to

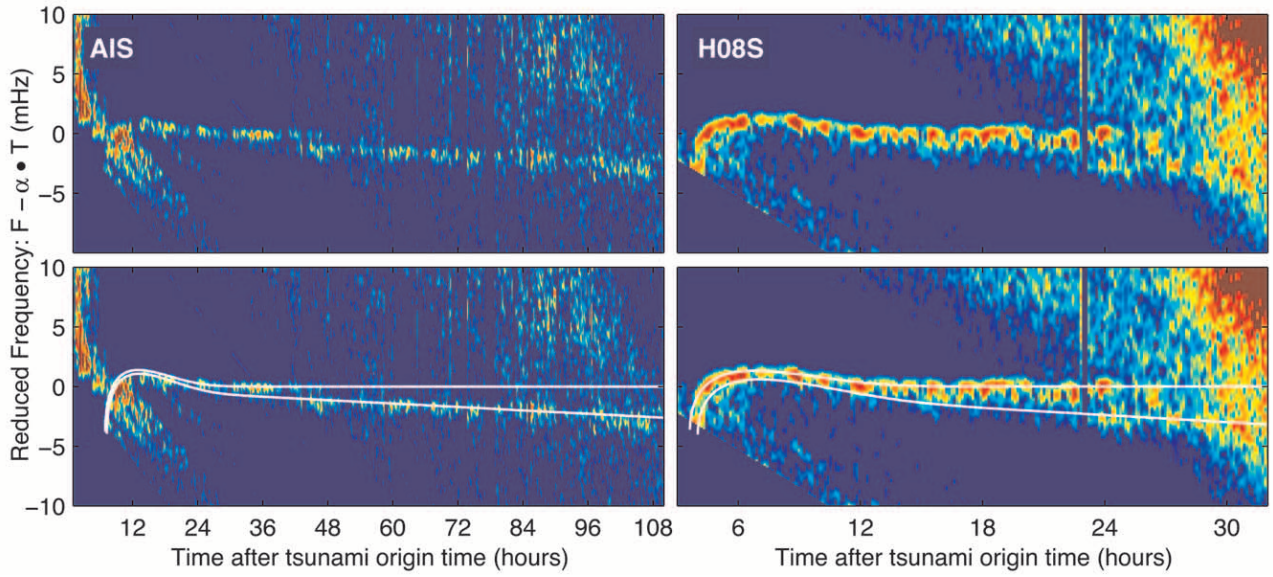

Figure 12. Fine-scale structure of the December 2004 tsunami. The spectrograms are plotted using a reduction frequency to enhance the separation between the arrivals. The top panels show just the data; the bottom panels have theoretical dispersion curves superimposed on the data. The reduction frequency factor α is the expected deep-water dispersion for the direct source, $g/4\pi\Delta$, where Δ is the source–receiver distance. Dispersion consistent with this factor would follow the zero line. Deviations from zero occur at the beginning of the signal because the deep-water approximation is not valid for the earlier (lower-frequency) arriving waves. Waves that have traveled further than the distance assumed for α will have a negative slope. Secondary arrivals can be distinguished from the direct arrival. Theoretical curves are for waves traveling distances of 4970 km and 5180 km for station AIS and distances of 2710 km and 3040 km for station H08S.

arrive from Sri Lanka at COCO, which constrains the northwest extent of the source. The data from the direct arrivals at H01W, AIS, and H08S are used to locate a point source. A least-squares fit is derived to determine the best fitting source location, which is 4.3° N, 93.8° E. This location is used to compute all direct arrival dispersion curves shown in the spectrogram plots.

The chirp signals that arrive following the first either may be direct waves from other source regions or reflected waves. Dispersion distances are estimated for these secondary chirps: three at H08S, one at H01W, and one at AIS (Table 3). Assuming direct propagation results in annuli similar to those used for the first arrival. Reflection locations will lie on an ellipse with the source location and station location acting as foci. These reflection locations, like the direct annuli, are determined using an ellipsoidal earth model. This is analogous to the method for reflection of *T* waves used in Hanson and Bowman (2006). Figure 15 shows possible source (left) or reflection (right) locations for the distinct chirps following the first arrivals.

The source or reflection locations are ambiguous because there are no azimuthal constraints, and it is not clear which signals to associate between stations. Assuming direct arrivals, the first AIS and H08S chirps coincide with an area just south of Great Nicobar Island near 6.5° N, 93.6° E. The other two chirps at H08S could correspond to an area at about 10° N. However, treating the secondary arrivals as reflections indicates that the chirps could just as easily correspond to reflections off Sumatra and the surrounding bathymetry.

An additional piece of information suggests the secondary AIS chirp is a direct tsunami wave. Figure 16a shows the spectrogram from AIS up to 100 mHz. The chirp has continuous energy to at least 60 mHz. On close examination, it is the second chirp and not the first arrival that continues to these high frequencies. This additional frequency content allowed for the higher resolution fit in Figure 13. The first arrival displays energy up to almost 30 mHz. If the second arrival were a reflection of the first, it would have similar or less bandwidth compared with the first. Because the opposite is true, the second arrival is likely a separately generated tsunami, rather than a reflection.

We hypothesize that this second signal originates from a source region that is shallower than the first source. The spectrum of the tsunami wave generated by a seafloor displacement depends on the ratio of the wavelength to water depth. Ward (2001) suggests that wavelengths less than three times the water depth do not contribute significantly to tsunami waves. Figure 16b shows the attenuation of a surface tsunami wave as a function of frequency for a series of dif-

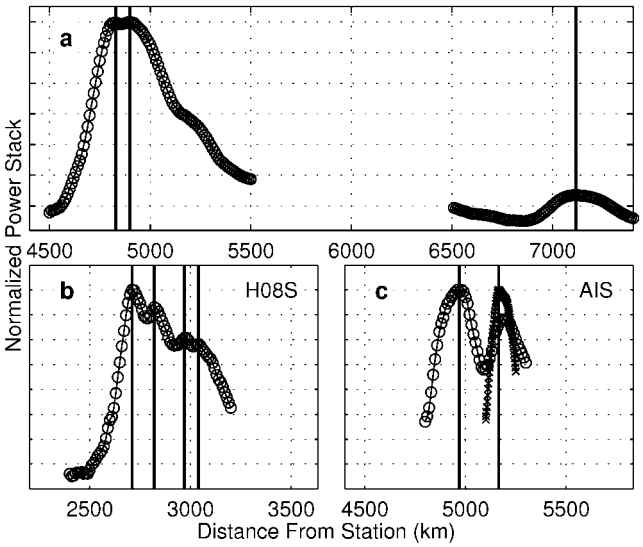

Figure 13. Power summation along theoretical dispersion curves for the December 2004 tsunami. Values of power spectra are summed between 8 and 30 mHz along theoretical dispersion curves for a 4500-m-deep ocean at a series of propagation distances. The results are normalized to the maximum value as a function of distance from the station. The peaks are interpreted as individual sources of tsunami energy or reflections of a tsunami wave. Vertical lines are drawn at individual peaks. The stack summation results for a later-arriving signal (reflection) at H01W is included and corresponds to the peak at 7115 km. The detailed structure in the main arrival at H08S and AIS can be seen in panels (b) and (c). The second curve (×) shown in (c) is a sum of the power between 10 and 60 mHz because this secondary signal observes higher-frequency energy than the other arrivals.

ferent water depths. There is a straightforward functional relationship between depth and frequency for any constant attenuation level. Namely, the depth is inversely proportional to the square of the frequency. To double the frequency content of a surface wave keeping all else equal requires reducing the depth by a quarter. This factor of four in depth does not include possible differences in the fault rupture at different locations. However, the frequency content of the second arrival does suggest a large difference in water depth at the source. An alternative hypothesis is that the secondary source had more energy at higher frequencies than the first source. We do not consider this likely because most seismic and tsunami estimated models show more slip in the first source area. Constraining the second source to shallow water and areas with direct paths to AIS places it just south of Great Nicobar Island.

Dispersed signals arriving significantly later than the first tsunami correspond to reflections from prominent bathymetric features in the Indian Ocean. Many signals have been identified at the hydrophone and seismic stations (Table 3). Coherent array processing of data from the H08S and H08N triads leads to azimuthal constraints of the largest reflections (Fig. 17). Using the distance constraints from the dispersion curves, and assuming the high-frequency tsunami source location determined earlier, ellipses representing potential reflection surfaces are computed (Fig. 18). Azimuth constraints are also included for the H08N reflector. Most of the reflection ellipses intersect prominent bathymetric features to the west of Sumatra. Reflections from Sri Lanka are seen at Cocos (Keeling) Islands and Cape Leeuwin, Australia. Many stations observe reflections off the Maldives and associated seamounts. Reflections from the Mascarene Plateau, near the Seychelles, are observed at Diego Garcia and Cocos (Keeling) Islands. A reflection that is likely from the Andaman Islands is observed at Cocos (Keeling) Islands. There is a small possibility that this reflection is actually from Christmas Island.

Discussion

The 26 December 2004 earthquake ruptured 1200–1300 km of the plate boundary, and the rupture process was complex (Ammon *et al.*, 2005). The largest slip occurred in the southern portion of the rupture zone, starting near the epicenter and continuing up to 200 km north of the epicenter. A gap of 250–400 km exists between the primary large slip zone and a second zone of slip. There is also a gap of 400 km between source locations of large amplitudes of *T* waves inferred from H08S hydroacoustic data (Guilbert *et al.*, 2005). The main destructive tsunami from the 26 December 2004 earthquake is primarily a low-frequency ($<$0.5 mHz) wave (Abe, 2006). This wave has very long wavelengths ($>$10 km at 4 km depth), interacts strongly with the seafloor, and has to be modeled using a continuous source consistent with the seismic rupture and propagated with a three-dimensional ocean (e.g., Fujii and Satake, 2007). Dispersive tsunami waves have been observed elsewhere but at frequencies and locations where interactions with bathymetry cannot be ignored (e.g., González and Kulikov, 1993). The high-frequency waves observed here quickly leave shallow water and can be successfully modeled using simple dispersion theory. The higher frequencies do not feel the ocean floor at all. The observations appear to be consistent with two discreet tsunami sources. This allowed us to locate the high-frequency tsunami sources with simple geometrical considerations.

The first high-frequency chirp signals observed on hydrophones and seismometers are consistent with a pointlike source tsunami. The chirps' narrow widths indicate a source region less than 30 km in diameter. The arrival times are also consistent with a point source. H08S bounds the western edge of the source region, H01W bounds the southern edge, and AIS bounds the region on the southwest side (Fig. 14). In addition, reflections observed at the Cocos (Keeling) Islands are consistent with a signal originating at ~4° N and reflecting from the steep continental shelf at the southeast edge of Sri Lanka. This observation, if correct, bounds the

Table 3
Distances Measured from Dispersed Waves

STA	Dispersed Distance (km)	Azimuth (deg)	Most Likely Source
H01W	4830 ± 15		Direct
	4900 ± 20		Direct or near-source reflection
	7115 ± 20		Sri Lanka reflection
	8200 ± 50		Maldives reflection
H08S	2710 ± 10	62.3 ± 1.8	Direct
	2820 ± 15		Direct or near-source reflection
	2970 ± 20		Near-source reflection
	3040 ± 20		Near-source reflection
	5800 ± 100	235 ± 30	Mascarene Plateau reflection
H08N	2840 ± 20		Direct or near-source reflection
	2910 ± 20		Diego Garcia or near-source reflection
	3000 ± 20		Maldives or near-source reflection
	3110 ± 20		Maldives or near-source reflection
	5225 ± 50		Mascarene Plateau (~10° S)
	5600 ± 50		Mascarene Plateau (~15° S)
	5850 ± 50	265 ± 20	Mascarene Plateau (~5° S)
	6050 ± 50	265 ± 20	Mahe, Seychelles reflection
AIS	4970 ± 25		Direct
	5180 ± 20		Direct or near-source reflection
	6500 ± 50		Maldives reflection
COCO	1900 ± 50		Direct
	3130 ± 50		Andaman Islands reflection
	4085 ± 50		Sri Lanka reflection
	5250 ± 15		Maldives reflection
	8800 ± 50		Mascarene Plateau reflection
RER	5150 ± 20		Direct (secondary source)

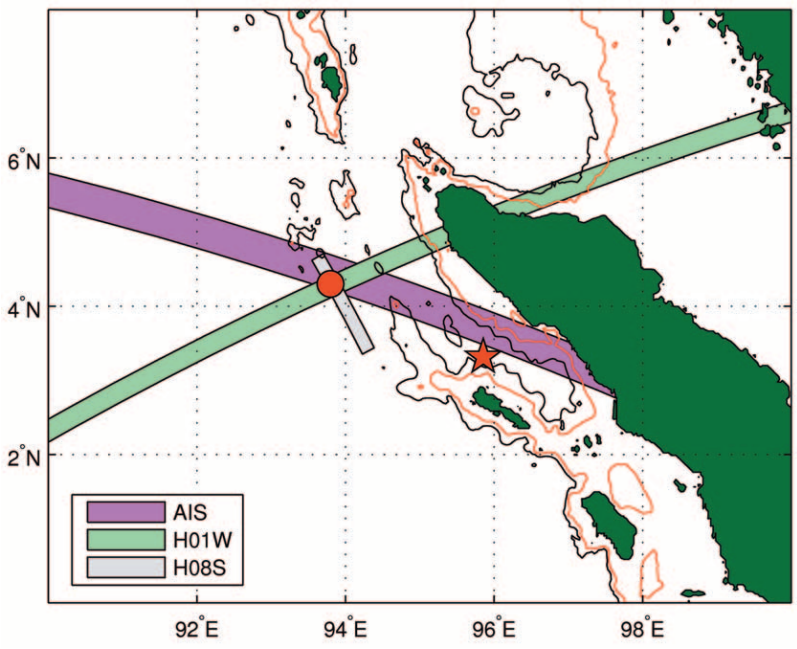

Figure 14. Possible source locations of the December tsunami determined from first arrivals. The distance from each station was determined from the best-fitting dispersion curve. The width of each patch is determined by the width of the peak in Figure 13. There is no azimuth information from AIS and H01W, so the possible source locations are defined by annulus equidistant from the station. The high-frequency (>18 mHz) FK results in Figure 10 are used to constrain the H08S annulus to a 4° arc. An ellipsoidal earth model was used for computing distances. The red dot indicates our best-fit source location. The red star is the epicenter of the December 2004 earthquake.

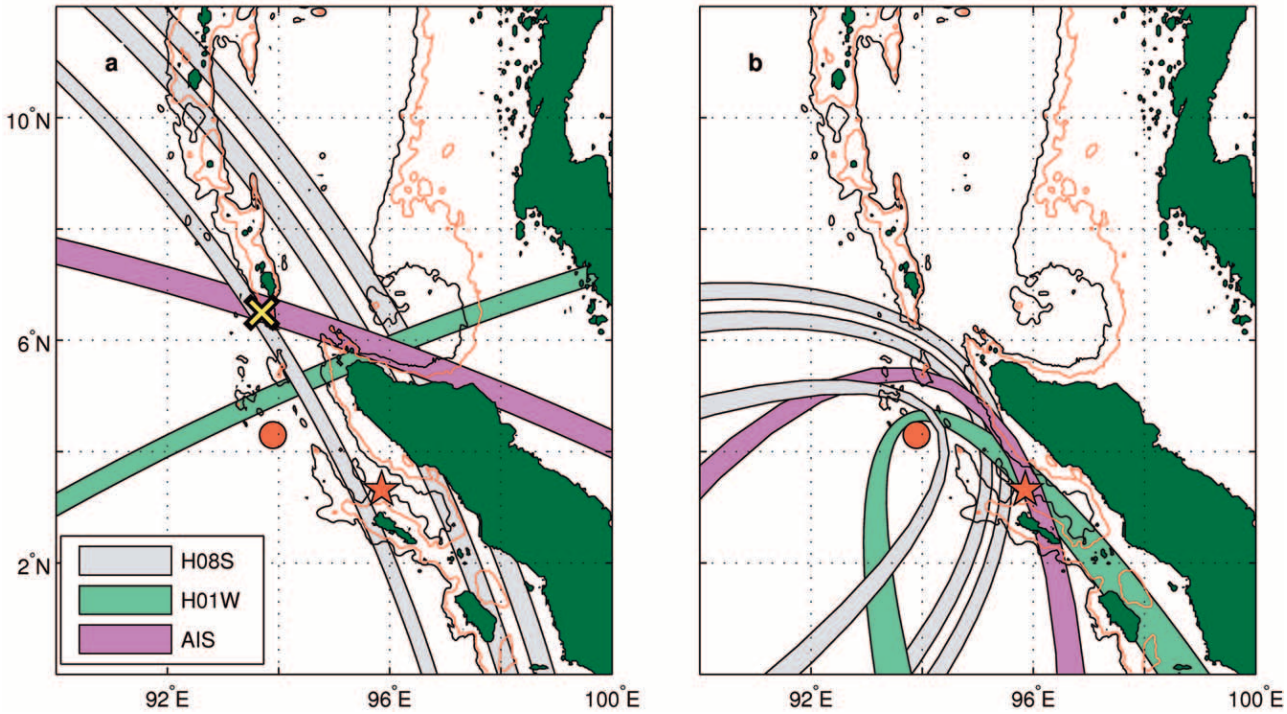

Figure 15. Possible source or reflection locations of the secondary high-frequency arrivals observed for the December tsunami. The secondary arrivals were identified in Figure 13. They may represent direct tsunami waves created at a different location than the first arrival, or they may be reflections of the first tsunami wave (or a combination of both). The red dot indicates the first-arrival source location (Fig. 14). Panel (a) shows the annuli of defining possible source locations assuming direct arrivals. Panel (b) shows possible reflection locations assuming arrivals are reflections from the first source location. Location differences between direct sources and reflected sources for the H01W secondary arrival are fairly minor. The secondary arrivals at H08S are more likely to be reflections off Sumatra or the surrounding islands than direct sources. Geometrically, the secondary AIS arrival is consistent with either a direct source or a reflection, but alternative evidence suggests that the arrival is a secondary source as opposed to a reflection (Fig. 16). The × indicates the possible location of a secondary source.

region on the northern side. Finally, secondary arrivals at H08S are consistent with reflections from Sumatra that bound the western edge of the region.

The location of the first high-frequency tsunami source is in the area of maximum slip as computed from seismic data (e.g., Ammon *et al.*, 2005; Lay *et al.*, 2005) or tide gauge and satellite measurements of the tsunami (e.g., Fine *et al.*, 2005; Song *et al.*, 2005; Hirata *et al.*, 2006; Fujii and Satake, 2007). The frequencies of the observations presented here are much higher than typically associated with tsunamis. Because high frequencies are attenuated by the water depth, it might be expected that the high-frequency source would correspond to the shallowest bathymetry. However, the location determined for the first high-frequency source does not correspond to the shallowest area in this high-slip region. This might indicate that there was especially large and concentrated seafloor uplift at the hypothesized source location.

A secondary source potentially identified, just south of Great Nicobar Island near 6.5° N, 93.6° E, corresponds to a high-slip area in some seismic models, in particular, slip models derived from teleseismic *SH* waveforms (Ammon *et al.*, 2005). One of the key observations that led to this interpretation is the 60-mHz signal observed at seismic station AIS. The 60-mHz (17-sec period) signal implies a source ocean depth of 200 m or less. This is consistent with significant vertical deformation in shallow water, as implied by the coseismic uplift of 1–2 m on the Andaman Islands and 1–4 m subsidence on the Nicobar Islands (Bilham *et al.*, 2005). The biggest problem with this interpretation is the lack of similar observations at other stations. Although signals are commonly observed to 30 mHz, AIS is the only station that observed 60-mHz signals. There are several reasons why this might be expected. The hydrophone stations are not expected to record these frequencies because at ~1300 m depth signals greater than 30 mHz are highly attenuated. Other seismic stations may not efficiently record the higher frequencies, or, in some cases (e.g., RER), we were only able to obtain data sampled at 0.1 Hz. AIS appears to be especially suited for recording ocean swells. For example,

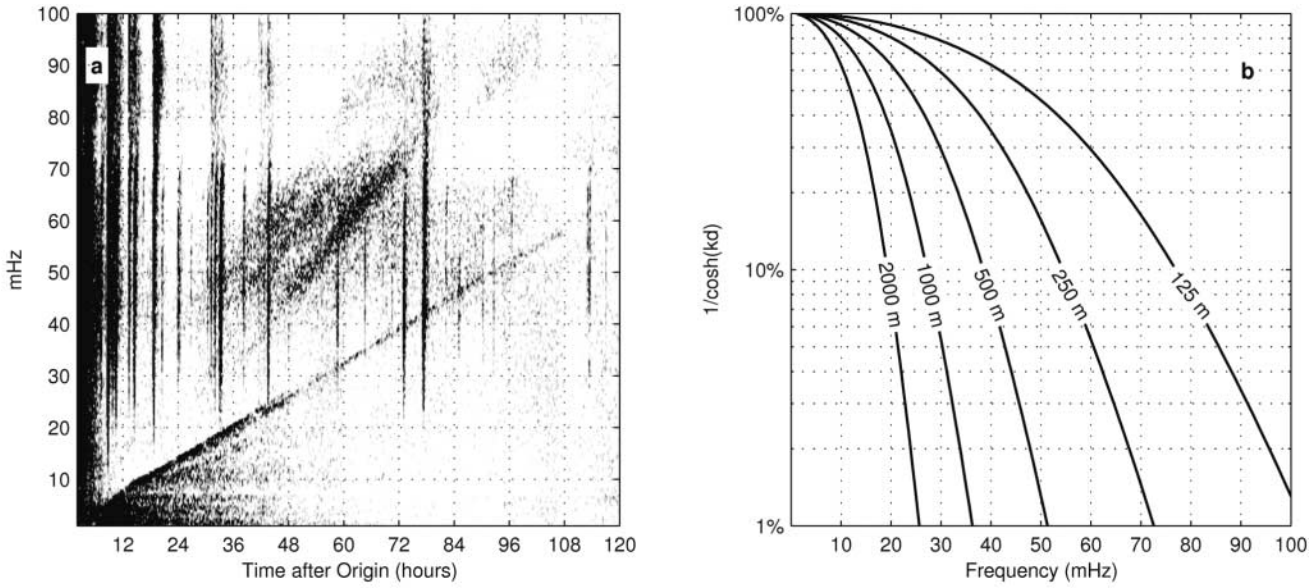

Figure 16. Evidence in the AIS signal of a secondary shallow source. (a) Extended spectrogram for seismic station AIS spanning a period of 5 days after the December 2004 earthquake. The dispersed tsunami signal is clearly visible to 60 mHz. Dispersive waves from cyclone Chambo between 50 and 100 mHz are visible starting 24 hr into spectrogram, which indicates that AIS is well situated to record ocean swell. The tsunami signal that extends to 60 mHz corresponds to the second arrival in Figure 13. The first arrival only extends to ~30 mHz. (b) The attenuation relation, 1/cosh(*kd*), for generation of surface waves from a seafloor source for water depths ranging from 125 to 2000 m. The attenuation with frequency is inversely proportional to the square root of the water depth, and therefore a factor of two decrease in frequency corresponds to a quadrupling of water depth. The frequency content of the second arrival indicates that it is not a reflection of the first, and that it originates from a shallower source region.

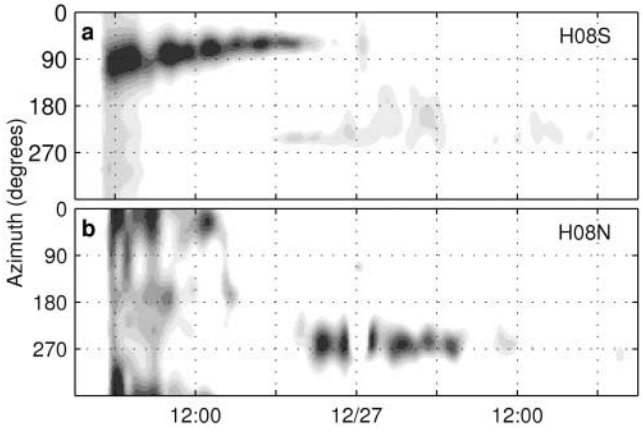

Figure 17. Time-bearing plots based on coherent processing for the two Diego Garcia hydroacoustic triads for the December 2004 tsunami (Hanson and Bowman, 2005). The principal tsunami signal at H08S has an azimuth that sweeps from 90° to 60° consistent with the earthquake location and possible refraction of lower frequencies by the Chagos Archipelago. The presence of the archipelago also explains the absence of a single, coherent direct signal at H08N. Secondary arrivals with bearings from 240 to 270° are interpreted to be reflections from the Mascarene Plateau. Lobes in the triad array responses cause artifacts at times less than 5 hr.

the prominent diagonal bands that arrive prior to the tsunami signal in Figure 16a coincide with expected waves from the tropical cyclone Chambo.

Fine *et al.* (2005) used tsunami arrival times measured at tide gauges and satellite altimetry to delineate the source region of the 26 December 2004 tsunami. They found two "hot spots" of wave generation separated by about 400 km within the larger tsunami source region. These hot spots produced two peak pulses of tsunami energy embedded in the tsunami wave train. The source areas are centered in an area of initial fast slip in the southern portion of the earthquake rupture zone and in an area of slower slip that occurred as the earthquake rupture propagated to the north. The tsunami sources of Fine *et al.* (2005) are located at approximately 4° N, 94° E and 10° N, 93° E. Our initial high-frequency tsunami source is consistent with their southern source area. Two of our later secondary arrivals observed at Diego Garcia are consistent with their 10° N location. However, our signals are also consistent with reflections of the first source from the coast of Sumatra. Because other evidence of a northern high-frequency source is lacking, we believe these secondary signals are more likely near-source reflections. This does not necessarily contradict Fine *et al.* (2005) because they are modeling the low-frequency signal as opposed to the high-frequency signals observed here. The tra-

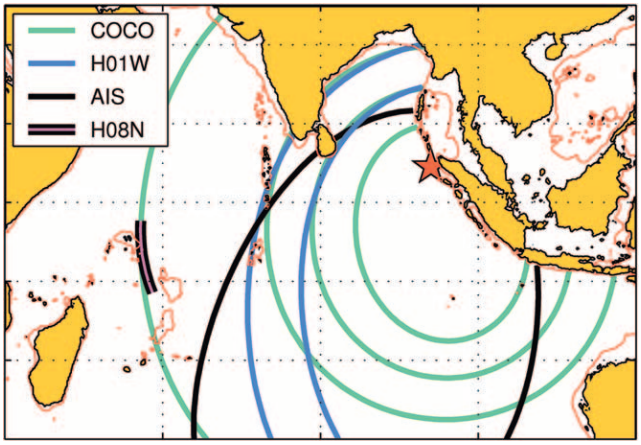

Figure 18. Map showing inferred location of reflections for the December tsunami. Light red lines correspond to the 500-m bathymetric contour. Total distance traveled is determined by fitting dispersion curves to the observed high-frequency tsunami signals (for examples, see Fig. 13). The source location used to compute possible reflector locations assuming an ellipsoidal earth was estimated from the direct arrivals (Fig. 14). The results are plotted as ellipses color coded by station. The azimuthal constraint from Figure 17 has been included for the reflection observed at H08N. The reflector locations can be inferred by locations of steep bathymetry and the main radiation pattern from the tsunami. Both H08N and COCO observed a reflection from a part of the Mascarene Plateau near the Seychelles. COCO, H01W, and AIS observed reflections from the Maldives (three different islands). COCO and H01W observe reflections from Sri Lanka. A fourth COCO reflection could be from either the Andaman Island chain or Christmas Island.

ditional tsunami observations record signals of less than 1 mHz. At those frequencies, the tsunami generation has to be treated as a complex broad-area source as opposed to the pointlike sources we infer from the high-frequency signals.

Yuan *et al.* (2005) also observed the tsunami signal on seismic stations in the Indian Ocean. They, however, examine the stronger low-frequency tsunami as opposed to the high-frequency dispersion presented here. Both this study and Yuan *et al.* support the conclusion that tsunami-induced seismic signals do not propagate very far from shore or to higher-elevation stations.

Tsunamis could generate the observed seismic signals by several possible mechanisms. Dahlen and Tromp (1998) discuss tsunamis in the framework of the Earth's normal modes. Oceanic surface-gravity waves can be considered a type of "exotic" spherical oscillation mode, which they refer to as tsunami modes. The displacement eigenfunctions of the tsunami modes are predominantly confined to the homogeneous ocean; at frequencies of 1 and 7 mHz the predicted displacements within the solid Earth are about 2 and 4 orders of magnitude smaller, respectively, than those in the overlying ocean (Dahlen and Tromp, 1998). Nevertheless, seismic signals from tsunamis fall directly out of the normal-mode framework. Yuan *et al.* (2005) suggest two alternatives. They note that the absence of tsunami energy on the vertical component and the rapid decay from the coast implies that the tsunami-induced seismic signals in the Indian Ocean may not be related to a propagating seismic wave. They also suggest that changes in sea level will cause changes of gravitational attraction to the seismometers or will tilt the coastal area. Although both gravitational pull and tilt may occur at the same time, they observe that the apparent direction of motion is perpendicular to the coastline, and this implies that tilt is the dominant mechanism. However, the observations at the higher frequencies are unlikely to be caused by tilt.

The IMS hydrophone triads have fortuitously provided a useful instrument to observe the Sumatra tsunamis. The triads' large sensor-separation design, unusual for hydroacoustic arrays, results in large apertures, which makes possible the array processing of the tsunami signal. The stations are in deep water, and thus the tsunami wave should not be as strongly distorted by the bathymetry that so often afflicts tide gauge signals. This relatively undistorted vector analysis made possible by the hydrophone stations could provide details of the tsunami wave that helps improve our understanding of their generation.

Summary

Multiple dispersive tsunami signals from the December 2004 earthquake have been observed on hydroacoustic and seismic stations in and around the Indian Ocean basin and as far away as the southern Atlantic Ocean. Two stations observe a high-frequency dispersive tsunami signal from the 28 March 2005 earthquake. The onset times of the first direct tsunami signals are consistent with the time of arrival observed on tide gauges or predicted from simple propagation models. The tsunami signals are dispersed from 1 to 30 mHz and in one case up to 60 mHz. The signals behave like shallow-water waves at their lowest frequencies and like deep-water waves at their highest frequencies. The dispersion is consistent with predictions for ocean-gravity waves across the observed frequency band. We estimated the distance traveled by measuring the amount of dispersion in each signal. Using distance estimates, azimuth estimates, and theoretical considerations, two sources of high-frequency tsunami signals have been indentified. The first is located at 4.3° N, 93.8° E. This corresponds to the largest slip from seismic-rupture models. The second source location is south of Great Nicobar Island near 6.5° N, 93.6° E and corresponds to a large slip area on some seismic-rupture models. Reflections of the high frequency tsunami signal are also observed. Using distances traveled estimated from the dispersion, we have identified many of the bathymetric features from which the waves reflected. Most of the reflections we observed come from areas west of Sumatra toward Somalia, such as the Maldives and the Mascarene Plateau.

Acknowledgments

Seismic data were retrieved from the Global Seismograph Network (GSN) and the GEOSCOPE network via the Incorporated Research Institutions for Seismology Data Management System (IRIS DMS). We thank Spiro Spiliopoulos for providing data from seismic station MAW, and we thank Norm Gholson for his help obtaining the hydrophone responses at Diego Garcia and Cape Leeuwin. We thank an anonymous reviewer whose thoughtful and thorough review substantially improved the article.

References

Abe, K. (2006). Dominant periods of the 2004 Sumatra tsunami and the estimated source size, *Earth Planets Space* **58,** 217–221.

Ammon, C. J., C. Ji, H.-K. Thio, D. Robinson, S. Ni, V. Hjorleifsdottir, H. Kanamori, T. Lay, S. Das, D. Helmberger, G. Ichinose, J. Polet, and D. Wald (2005). Rupture process of the 2004 Sumatra-Andaman earthquake, *Science* **308,** 1133–1139.

Bilham, R., R. Engdahl, N. Feldl, and S. P. Satyabala (2005). Partial and complete rupture of the Indo-Andaman plate boundary 1847–2004, *Seism. Res. Lett.* **76,** 299–311.

Dahlen, F. A., and J. Tromp (1998). *Theoretical Global Seismology*, Princeton University Press, Princeton, New Jersey, 315–318.

de Groot-Hedlin, C. D. (2005). Estimation of the rupture length and velocity of the Great Sumatra earthquake of Dec 26, 2004 using hydroacoustic signals, *Geophys. Res. Lett.* **32,** L11303, doi 10.1029/2005GL022695.

Fine, I. V., A. B. Rabinovich, and R. E. Thomson (2005). The dual source region for the 2004 Sumatra tsunami, *Geophys. Res. Lett.* **32,** L16602, doi 10.1029/2005GL023521.

Fujii, Y., and K. Satake (2007). Tsunami source of the 2004 Sumatra-Andaman earthquake inferred from tide gauge and satellite data, *Bull. Seism. Soc. Am.* **97,** no. 1A, S192–S207.

Garcés, M., P. Caron, C. Hetzer, A. Le Pichon, H. Bass, D. Drob, and J. Bhattacharyya (2005). Deep infrasound radiated by the Sumatra earthquake and tsunami, *EOS Trans. AGU* **86,** 317.

González, F. I., and Y. A. Kulikov (1993). Tsunami dispersion observed in the deep ocean, in *Tsunamis in the World*, S. Tinti (Editor), Kluwer Academic, Dordrecht, The Netherlands, 7–16.

Gower, J. (2005). Jason 1 detects the December 26 2004 tsunami, *EOS Trans. AGU* **86,** 37–38.

Graeber, F. M., P. Grenard, and K. Koch (2005). Observations at IMS hydrophone stations from the December 2004 Indian Ocean tsunami event, *Geophys. Res. Abstr.* **7,** 08773.

Guilbert, J., J. Vergoz, E. Schisselé, A. Roueff, and Y. Cansi (2005). Use of hydroacoustic and seismic arrays to observe rupture propagation and source extent of the M_w = 9.0 Sumatra earthquake, *Geophys. Res. Lett.* **32,** L15310, doi 10.1029/2005GL022966.

Hanson, J. A., and J. R. Bowman (2005). Dispersive and reflected tsunami signals from the 2004 Indian Ocean tsunami observed on hydrophones and seismic stations, *Geophys. Res. Lett.* **32,** L17606, doi 10.1029/2005GL023783.

Hanson, J. A., and J. R. Bowman (2006). Methods for monitoring hydroacoustic events using direct and reflected T waves in the Indian Ocean, *J. Geophys. Res.* **111,** B02305, doi 10.1029/2004JB003609.

Hanson, J. A., R. Bowman, and G. Beall (2002). An advanced concept demonstration for monitoring the Indian Ocean, in *Proceedings of the 24th Annual Seismic Research Review*, Ponte Verde, Florida, 17–19 September 2002, 632–642.

Hirata, K., K. Satake, Y. Tanioka, T. Kuragano, Y. Hasegawa, Y. Hayashi, and N. Hamada (2006). The 2004 Indian Ocean tsunami: tsunami source model from satellite altimetry, *Earth Planets Space* **58,** 195–201.

Kulikov, E. (2005). Dispersion of the Sumatra tsunami waves in the Indian Ocean detected by satellite altimetry, Report from P.P. Shirshov Institute of Oceanology, Russian Academy of Sciences, Moscow.

Lamb, H. (1932). *Hydrodynamics*, Sixth Ed., Cambridge Univ. Press, New York, 738 pp.

Lay, T., and T. Wallace (1995). *Modern Global Seismology*, Academic Press, New York, 188.

Lay, T., H. Kanamori, C. J. Ammon, M. Nettles, S. N. Ward, R. C. Aster, S. L. Beck, S. L. Bilek, M. R. Brudzinski, R. Butler, H. R. DeShon, G. Ekström, K. Satake, and S. Sipkin (2005). The great Sumatra-Andaman earthquake of 26 December 2004, *Science* **308,** 1127–1133, doi 10.1126/science.1112250.

Merrifield, M. A., Y. L. Firing, T. Aarup, W. Agricole, G. Brundrit, D. Chang-Seng, R. Farre, B. Kilonsky, W. Knight, L. Kong, C. Magori, P. Manurung, C. McCreery, W. Mitchell, S. Pillay, F. Schindele, F. Shillington, L. Testut, E. M. S. Wijeratne, P. Caldwell, J. Jardin, S. Nakahara, F.-Y. Porter, and N. Turetsky (2005). Tide gauge observations of the Indian Ocean tsunami, December 26, 2004, *Geophys. Res. Lett.* **32,** L09603, doi 10.1029/2005GL022610.

Okal, E. A., J. Talandier, and D. Reymond (2006). Quantification of hydrophone records of the 2004 Sumatra tsunami, *Pure Appl. Geophys.* (in press).

Oltman-Shay, J., and R. T. Guza (1987). Infragravity edge wave observations on two California beaches, *J. Phys. Oceanogr.* **17,** 644–663.

Piatanesi, A., and S. Lorito (2007). Rupture process of the 2004 Sumatra-Andaman earthquake from tsunami waveforms inversion, *Bull. Seism. Soc. Am.* **97,** no. 1A, S223–S231.

Song, Y. T., C. Ji, L.-L. Fu, V. Zlotnicki, C. K. Shum, Y. Yi, and V. Hjorleifsdottir (2005). The 26 December 2004 tsunami source estimated from satellite radar altimetry and seismic waves, *Geophys. Res. Lett.* **32,** L20601, doi 10.1029/2005GL023683.

Tanioka, Y., Yudhicara, T. Kususose, S. Kathiroli, Y. Nishimura, S. Iwasaki, and K. Satake (2006). Rupture process of the 2004 great Sumatra-Andaman earthquake estimated from tsunami waveforms, *Earth Planets Space* **58,** 203–209.

Titov, V. I., A. B. Rabinovich, H. O. Mofjeld, R. E. Thomson, and F. I. González (2005). The global reach of the 26 December 2004 Sumatra tsunami, *Science* **309,** 2045–2048, doi 10.1126/science.1114576.

Tolstoy, M., and D. R. Bohnenstiehl (2005). Hydroacoustic constraints on the rupture duration, length, and speed of the great Sumatra-Andaman earthquake, *Seism. Res. Lett.* **76,** 419–425.

Ward, S. W. (2001). Tsunamis, in *Encyclopedia of Physical Science and Technology*, Third Ed., Academic Press, New York.

Webb, S., X. Zhang, and W. Crawford (1991). Infragravity waves in the deep ocean, *J. Geophys. Res.* **96,** 2723–2736.

Yuan, X., R. Kind, and H. A. Pedersen (2005). Seismic monitoring of the Indian Ocean tsunami, *Geophys. Res. Lett.* **32,** L15308, doi 10.1029/2005GL023464.

Science Applications International Corporation
Monitoring Systems Division
San Diego, California 92121

Manuscript received 4 January 2006.